Supporting Information

Content

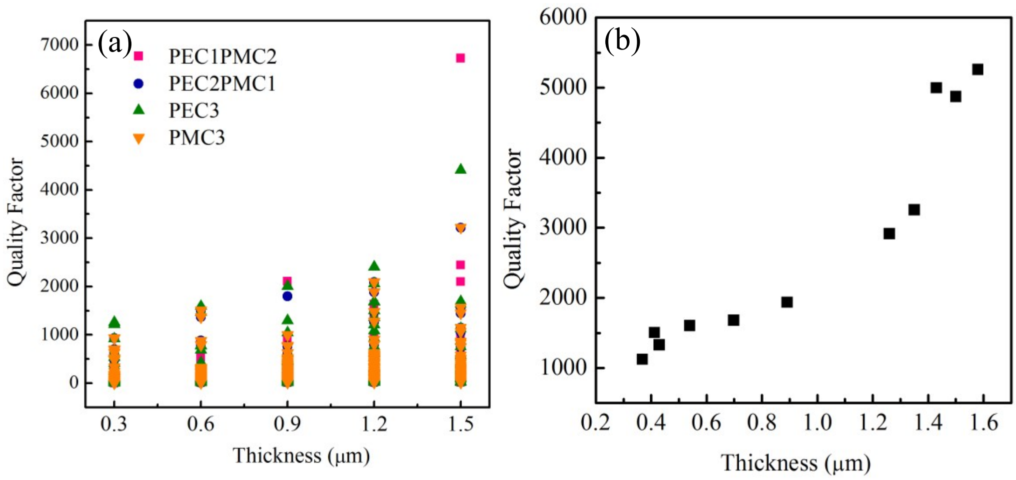

Fig. S1 (a) The relation between thickness of microcavity and Q-factor is simulated by the three-dimensional finite element method (FEM) (COMSOL Multiphysics 5.0). (b) Experimental relation between thickness of microcavity and Q-factor.

The relation between thickness of microcavity and Q-factor is simulated by the three-dimensional finite element method (FEM) (COMSOL Multiphysics 5.0). Due to the symmetry of the cube, only one-eighth of the cube needs to be simulated by setting four different boundary conditions. The boundary condition of a plane is set as a perfect electrical conductor (PEC) corresponding to a symmetric mode, or a perfect magnetic conductor (PMC) corresponding to an antisymmetric mode. Three symmetric planes are utilized to satisfy the limitation of the computer's RAM. We set the edge length as 1.5 μm and simulate five different thickness of cavity, which shown as Figure S1a. From the theoretical simulation, it can be seen that with increasing the thickness of the cavity, the theoretical Q-factor increases. And, as the thickness of the cavity increases to 1.5 μm, the micro-cubic cavity with three same edges length has the highest Q-factor. Hence, the increase of Q-factor is due to the increase of thickness of the microcavities can be theoretically proved. In the experiment, we also measured the Q-factor of microcavities which have nearly same edge length of 1.5 μm but different thickness. The result shown in Figure S1b manifests that the Q-factor increases with the increasing of thickness, which is in agreement with the theoretical result.

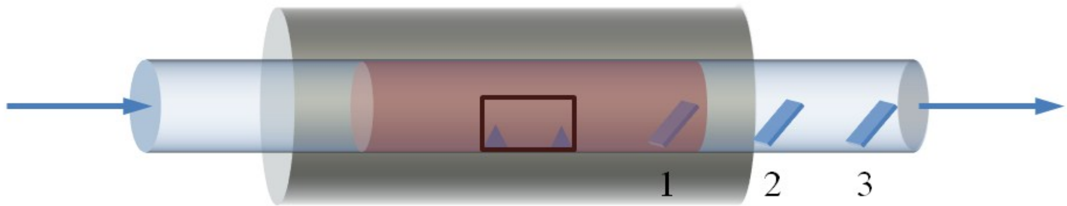

Fig. S2 Diagrammatic drawing of one-step dual-source chemical vapor deposition system. Three silicon wafers (1, 2, 3) are placed in the outlet at different postitions.

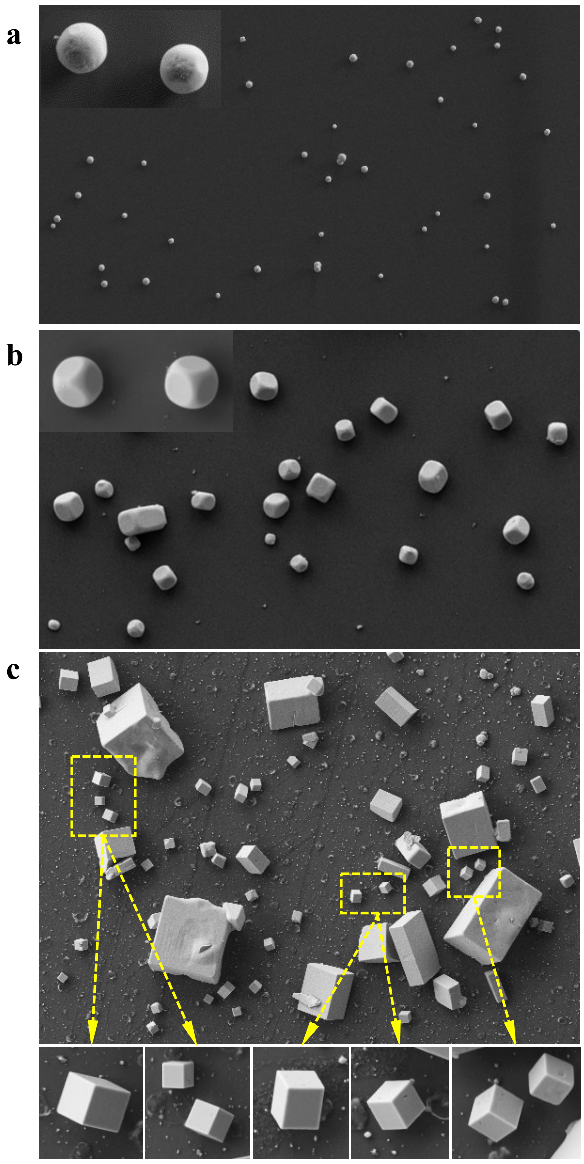

Fig. S3 SEM images of microcavities in (a) Si wafer 3, (b) Si wafer 2, (c) Si wafer 1.

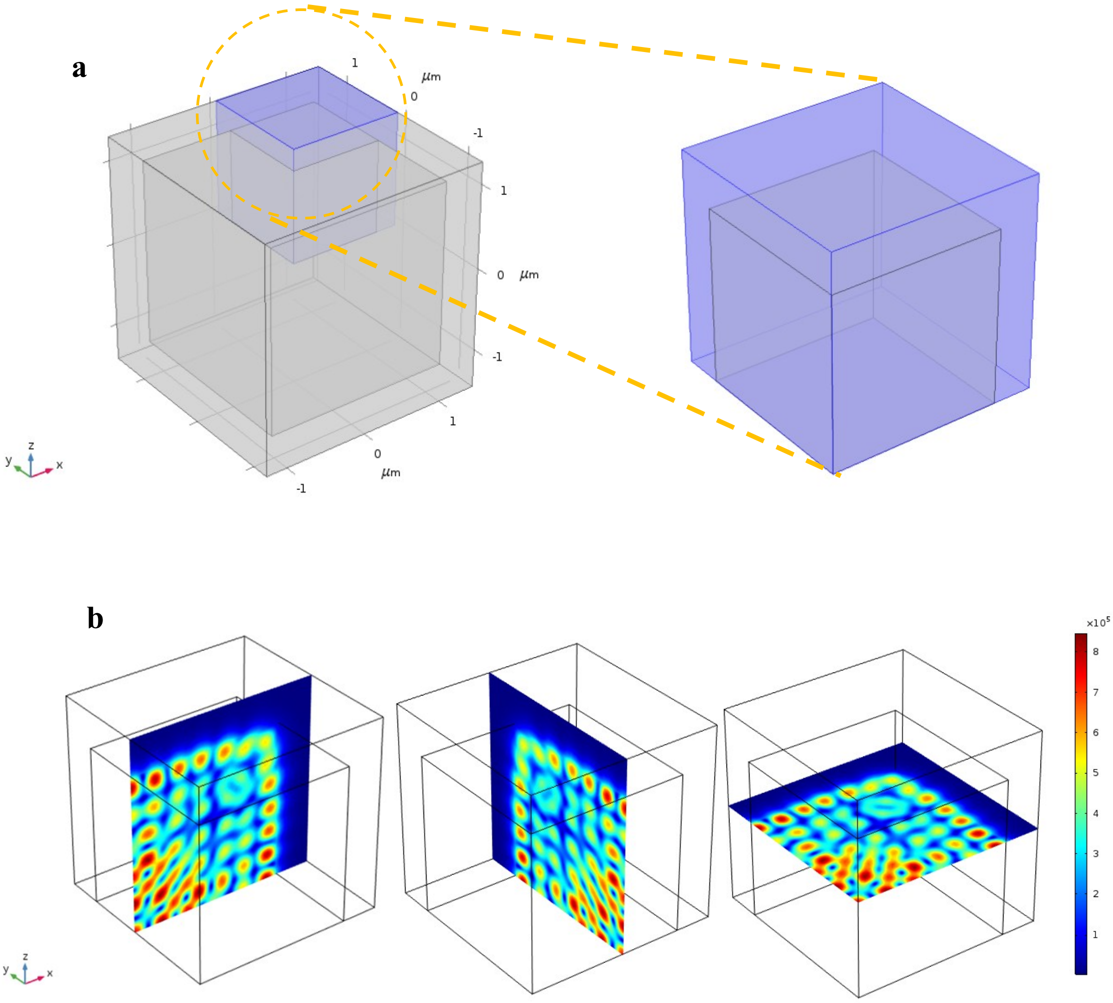

Fig. S4 (a) Structure of 3D simulation. (b) Mode field distribution of the high Q mode on three different planes, x-y plane, y-z plane and x-z plane.

As shown in Fig. S4a, we set the microresonator to have a side length of 2.2 μm and a vacuum layer thickness of 0.25 μm. Since the cube is completely symmetric about the three faces that pass its center (e.g. x-y, y-z, x-z), we can reduce the amount of calculation by setting the appropriate boundary conditions. At the same time, each symmetry plane has two boundary settings, namely a perfect electrical conductor (PEC, corresponding to a symmetric mode) and a perfect magnetic conductor (PMC, corresponding to an antisymmetric mode). Therefore, there are four different combinations to completely simulate the mode of a cubic microresonator. Therefore, there are four different combinations to completely simulate the mode of a cubic micro-resonator where all three symmetry planes are perfect electrical conductors

(PEC3), the two symmetry planes are perfect electrical conductors and one symmetry plane is a perfect magnetic conductor (PEC2-PMC1), one symmetry plane is a perfect electrical conductor and two symmetry planes are perfect magnetic conductors (PEC1-PMC2), and all three symmetry planes are perfect magnetic conductors (PMC3). Fig. S4b shows the mode field distribution of the high Q mode on three planes. All three symmetry planes are set to perfect electrical conductors, so the mode field distribution $|H|^2$ of the three planes is exactly the same.

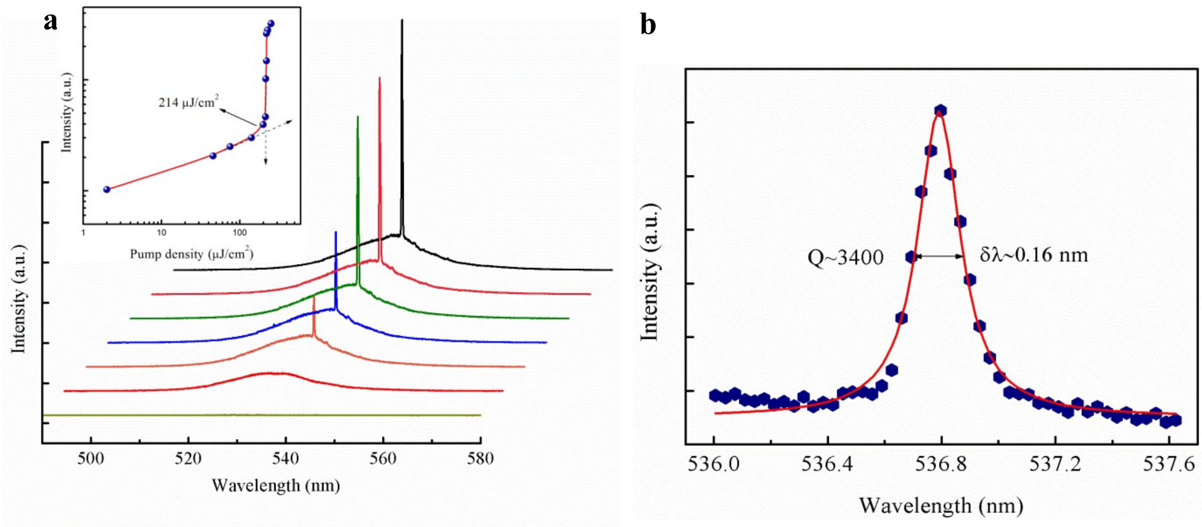

Fig. S5 Single-mode lasing obtained from an individual $CsPbBr_3$ MCC at room temperature through 355 nm nanosecond laser (1.1 ns, 20 KHz). (a) Excitation power-dependent lasing spectra from one single $CsPbBr_3$ MCC. (b) Lorentz fitting of a lasing oscillation mode, giving the FWHM of the lasing peak (δλ) ~0.16 nm.

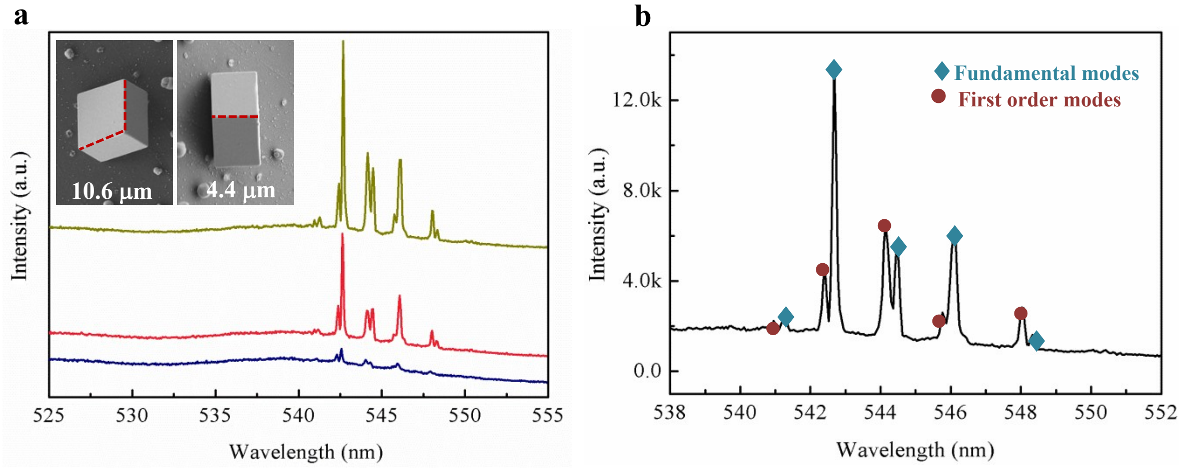

Fig. S6 Multi-mode lasing spectra with sub-modes. (a) Lasing obtained from large $CsPbBr_3$ MCC. Insets: SEM imges of large $CsPbBr_3$ MCC with three sides' length of 10.6 μm, 10.6 μm and 7.4 μm. (b) Enlarged lasing spectra.

Material	Lasing peak (nm)	Lasing linewidth (nm)	Q-factor	Threshold at RT ($\mu J/cm^2$)	Pumping Source
[1] ZnSe Nanowire	461	0.72	640	~340	150 fs, 1 kHz
[2] CdS Nanowire	512	0.40	1280	~14	120 fs, 1 kHz
[3] ZnO Nanowire	387	0.80	484	~400	8 ns, 10 Hz
[4] ZnO Nanodisk	389	0.70	556	~750	8 ns, 10 Hz
[5] $CsPbCl_3$ Nanowires	420	0.30	1400	~7.0	150 fs, 100 kHz
[6] $CsPbBr_3$ Nanowires	538	0.26	2069	~6.2	100 fs, 250 kHz
[7] $CsPbBr_3$ Nanoplatelet	535	0.15	3500	~2.0	50 fs, 1 KHz
[8] $CsPbBr_3$ Microsphere	545	0.09	6100	~0.42	40 fs, 10 KHz
[9] $CsPbBr_3$ Nanocuboid	539	0.29	1850	~40.2	35 fs, 1 KHz
[♦] $CsPbBr_3$ MCC	541	0.064	8500	~16.9	40 fs, 10 KHz
[♦] $CsPbBr_3$ MCC	537	0.16	3400	~214	1.1ns, 20 KHz

Table S1. Comparisons of main laser parameters of reported semiconductor nano/microcavity laser. [♦] represents the work of this paper.

References

[1] Xing. G, Luo. J, Li. H, Wu. B, Liu. X, Huan. A, Fan. H, T. C. Sum, *Adv. Opt. Mater.* 2013, ***1***, 319−326.

[2] Pan. A, Liu. R, Yang. Q, Zhu. Y, Yang. G, Zou. B, Chen. K, *J. Phys. Chem. B*. 2005, ***109***, 24268−24272.

[3] Gargas. D. J, Toimilmolares. M. E, Yang. P, *J. Am. Chem. Soc.* 2009, ***131***, 2125−2127.

[4] Gargas. D. J, Moore. M. C, Ni. A, Chang. S. W, Zhang. Z, Chuang. S. L, Yang. P, *ACS Nano*, 2010, ***4***, 3270−3276.

[5] Park. K, Lee. J. W, Kim. J. D, Han. N. S, Jang. D. M, Jeong. S, Park. J, Song. J. K. J, *Phys. Chem. Lett.* 2016, ***7***, 3703−3710.

[6] Fu. Y, Zhu. H, Stoumpos. C. C, Ding. Q, Wang. J, Kanatzidis. M. G, Zhu. X, Jin. S, *ACS Nano*, 2016, ***10***, 7963−7972.

[7] Q. Zhang, R. Su, X. Liu, J. Xing, T. C. Sum, Q. Xiong, *Adv. Funct. Mater*. 2016, ***26***, 6238-6245.

[8] B. Tang, H. Dong, L. Sun, W. Zheng, Q. Wang, F. Sun, X. Jiang, A. Pan. L. Zhang, *ACS Nano*, 2017, ***11***, 10681-10688.

[9] Z. Liu, J. Yang, J. Du, Z. Hu, T. Shi, Z. Zhang, Y. Liu, X. Tang, Y. Leng, R. Li, *ACS Nano.* 2018